

# Probing the Interface Evolution in Co-sintered All-Phosphate Cathode-Solid Electrolyte Composites

Michael Malaki, Johannes Haust, Jean Philippe Beaupain, Henry Auer, Andreas Beyer, Katja Wätzig, Mihails Kusnezoff, and Kerstin Volz\*

To achieve cohesive interfaces of solid components in next-generation Li-ion batteries (LIBs) composed of oxide cathodes and solid electrolytes (SEs) high-temperature sintering is necessary which leads to material degradation and phase decompositions. Thermochemically compatible components can address these issues. In this work, advanced electron microscopy techniques are employed to investigate the structural and chemical evolution taking place at the interfaces between a  $\text{LiFePO}_4$  (LFP) cathode and an in-house optimized  $\text{Li}_{1.3}\text{Al}_{0.3}\text{Ti}_{1.7}(\text{PO}_4)_3$  (LATP) SE co-sintered between 650 °C – 850 °C. While the LFP particles exhibit excellent structural stability, the LATP particles phase transforms at elevated temperatures. At 650 °C,  $\text{Fe}_{\text{Li}}$  anti-site defect is observed at the LFP grain boundaries. Between 750 and 850 °C, the LATP (R-3c) transforms into two orthorhombic phases (*Pbca* and *Pbcn*) of the type  $\text{Li}_{1.3+x}\text{Al}_{0.3}\text{Fe}_x\text{Ti}_{1.7-x}(\text{PO}_4)_3$  depending on Fe substitution while forming the cohesive interfaces. The discharge capacity of the composite decreases from 148 mAh g<sup>-1</sup> at 650 °C to 130 mAh g<sup>-1</sup> at 850 °C confirming that the new phases are still electrochemically active. This study provides a spatially resolved insight into the formation of cohesive interfaces highlighting the advantage of employing components with similar anionic structures for further improvements in LIBs.

to overcome the current thresholds of safety and energy density by replacing the organic liquid electrolytes with inorganic solids or polymers that can offer better performance over a wide range of operating temperatures. One such advancement is the development of an all-solid-state battery system consisting of a  $\text{Li}^+$  conducting solid electrolyte (SE) that can double up as a separator between an energy-dense cathode composite and a high-specific capacity anode such as lithium metal.<sup>[3,4]</sup> To realize the required energy densities and in turn the commercialization of these systems, the SEs have to be electrochemically, chemically, and mechanically compatible with the electrodes. Thus, it follows that SEs should be chemically stable against the lithium anode and at the same time possess similar lithium-ion dynamics as the cathode to provide the required electrochemical performance. Moreover, the SEs should have mechanical properties that make their synthesis and application into the current state-of-the-art battery systems

## 1. Introduction

The feasibility of Li-ion energy storage devices for electric vehicle applications has increased the demand for higher energy density, power density, and improved safety in these battery systems.<sup>[1,2]</sup> This has led to the rapid development of advanced battery devices

cost-effective by relying on existing large-scale electrode processing technology.<sup>[5]</sup>

Thiophosphate-based SEs offer high-ionic conductivity (1 – 10 mS cm<sup>-1</sup>) and are extremely ductile and can be processed with electrode materials by simple mechanical pressing thus fulfilling both the electrochemical and mechanical requirements.<sup>[6]</sup> However, to ensure proper contact with the electrodes, the pressure has to be maintained throughout its cycle life.<sup>[1]</sup> The sensitivity of the thiophosphate SEs to ambient air and moisture makes it inherently expensive to process and also unsafe to operate due to the evolution of toxic  $\text{H}_2\text{S}$ .<sup>[7]</sup> The preparation, challenges, and design strategies for solid-state batteries with sulfide electrolytes are comprehensively reviewed in the following references.<sup>[8]</sup> Polymer SEs have shown improved ionic conductivities in recent years and can compensate for volumetric changes in the electrodes due to their elastic and plastic properties but fall short in the areas of rate capabilities and the need for high operating temperatures (> 60 °C) to reach the conductivities required to compete with the current-state-of-the-art.<sup>[9]</sup> In contrast to the above material systems, oxide SEs are more stable in the ambient atmosphere and provide high ionic conductivities in the order of 1 mS cm<sup>-1</sup>. Their rigid nature, however, makes high-temperature

M. Malaki, J. Haust, A. Beyer, K. Volz  
Materials Sciences Center (WZMW) and Department of Physics  
Philipps University of Marburg  
Hans Meerwein Strasse 6, 35032 Marburg, Germany  
E-mail: kerstin.volz@physik.uni-marburg.de  
J. P. Beaupain, H. Auer, K. Wätzig, M. Kusnezoff  
Fraunhofer Institute for Ceramic Technologies and Systems IKTS  
Winterbergstrasse 28, 01277 Dresden, Germany

The ORCID identification number(s) for the author(s) of this article can be found under <https://doi.org/10.1002/admi.202300513>

© 2023 The Authors. Advanced Materials Interfaces published by Wiley-VCH GmbH. This is an open access article under the terms of the Creative Commons Attribution License, which permits use, distribution and reproduction in any medium, provided the original work is properly cited.

DOI: 10.1002/admi.202300513

sintering necessary to form ion-conductive pathways within the SE and ensure sufficient contact with the active materials. Nevertheless, they do not require further mechanical support after the heat treatment.<sup>[10]</sup>

The interface between cathodes and oxide SEs plays a significant role in cell performance. While a lack of contact between the two components leads to large impedance and polarization losses, the use of elevated sintering temperatures to improve the contact surface area can result in the formation of new phases due to elemental interdiffusion that significantly alters the ionic conductivities.<sup>[3,11]</sup> Thus, it follows that materials with similar crystal structures and chemical compositions are to be employed to ensure both chemical and thermal stabilities during sintering. In this regard, composites based on oxide/phosphate solid electrolytes with commercially established oxide/phosphate cathodes are an ideal material system for practical consideration.<sup>[11,12]</sup> The current Li-ion battery architecture employs either layered cathodes based on LiNiO<sub>2</sub> (LNO) or olivine cathodes such as LiFePO<sub>4</sub> (LFP). The LNO delivers an extremely high specific capacity (> 220 mAh<sup>-1</sup>) but is not commercialized due to intermixing of the Li/Ni which leads to rapid capacity decay. Thus Ni-rich systems employing Co and Mn with the general formula LiNi<sub>x</sub>Co<sub>y</sub>M<sub>1-x-y</sub>O<sub>2</sub> (M = Al, Mn) named NCA/NCM are used to provide the necessary cycle life while still delivering comparable capacities. These Ni-rich cathodes are, however, highly unstable when de-lithiated at elevated temperatures. In contrast, the LFP is stable at high temperatures even when de-lithiated. Carbon-coated LFPs enable high charging rate and specific capacity (≈160 mAh g<sup>-1</sup>) while at the same time are environmentally less taxing when compared to Co-containing NCM/NCAs.<sup>[13,14]</sup>

Several studies have examined the interface stability of these cathode active materials (CAMs) with solid electrolytes such as lithium aluminum titanium phosphate (LATP) and lithium lanthanum zirconium oxide (LLZO).<sup>[11,15–17]</sup> The LATP SE exhibits high ionic conductivity (1 mS cm<sup>-1</sup>) and requires less demanding processing conditions (lower sintering temperature) with inexpensive starting materials as compared to LLZO. Studies combining X-ray diffraction (XRD) and thermal analysis in which the cathodes and solid electrolytes were co-sintered show that, subject to a sintering atmosphere, olivine cathodes offer better thermo-chemical compatibility with LATP than LLZO.<sup>[15,16]</sup> Computational studies, in addition, suggest that layered cathodes are more chemically compatible with LLZO than phosphate-based SEs.<sup>[11,18]</sup> On the experimental side, depositing NCM333 (LiNi<sub>1/3</sub>Co<sub>1/3</sub>Mn<sub>1/3</sub>O<sub>2</sub>) thin films on LATP substrate using pulsed laser deposition between 700 °C – 900 °C showed that Co interdiffuses into the LATP at both temperatures.<sup>[19]</sup> Here, scanning transmission electron microscopy energy dispersive X-ray (STEM-EDX) and electron energy loss spectroscopy analysis show that Co tends to accumulate at the cathode-solid electrolyte (CSE) interface at 900 °C forming Li-free Co-rich compounds. In our previous work, we examined the thermal stability of Ni-rich layered cathode NCM622 co-sintered with the LATP SE in the temperature range of 550 °C– 650 °C using advanced STEM imaging and analytical techniques.<sup>[20,21]</sup> We found that the microstructure of the cathode at the interfaces undergoes drastic phase transitions from layered to rock-salt compounds. In addition, volumetric changes result in cracks and material disintegration due to the continuous evolution of lithium and oxygen dur-

ing the heat treatment. Within the LATP, the Ti phase separates to form core-shell structures that impede the densification of the interfaces. These results further suggest that the anionic similarity between the cathodes and solid electrolytes plays a much more significant role in determining the thermochemical and mechanical compatibility of the interfaces.

The electrochemical and thermochemical compatibility between LFP and LATP has been previously investigated.<sup>[16,17,22]</sup> It is seen from these studies that at the macroscale, the CSE interfaces are compatible up to a temperature of 775 °C when co-sintered in Ar atmosphere.<sup>[22]</sup> Above 800 °C in an inert atmosphere (Ar/N<sub>2</sub>), multiple secondary phases are formed, a majority portion of which conforms to the type Li<sub>2</sub>M(PO<sub>4</sub>)<sub>3</sub> while in the O<sub>2</sub> atmosphere secondary phases of the type Li<sub>3</sub>M<sub>2</sub>(PO<sub>4</sub>)<sub>3</sub> start forming well below 500 °C (M can comprise of multiple elements of Al, Fe, Ti).<sup>[16,17]</sup> To determine the precise phases and gain additional insights into the structural evolution taking place at the CSE, a detailed microstructural investigation using advanced STEM techniques is warranted. These techniques will provide the necessary spatial resolution and control over beam doses to prevent any beam-induced degradations at the interfaces which typically have low electronic conductivities. Accordingly, in the current study, we investigate the microstructure of CSE interfaces of LFP and LATP co-sintered between 650 °C – 850 °C. To this end, we use high-resolution STEM (HRSTEM) to visualize the crystal structure of the cathodes, STEM-EDX to trace the chemical evolution at the interfaces, and automated-crystal orientation mapping TEM (ACOM-TEM) in combination with HRSTEM to identify and visualize the phases which promote the formation of cohesive interfaces in the temperature regime.

## 2. Results and Discussion

### 2.1. Morphology of Pristine LFP-LATP Composites

Figure 1 shows SEM micrographs visualizing the surface morphology of carbon-coated pristine LFP CAM and LFP-LATP CSE composites co-sintered between 650 and 850 °C. The pristine CAM consists mostly of primary particles with dimensions ranging between ≈ 0.5 to 2 μm. As marked by the dashed orange enclosures in Figure 1a, some of these particles tend to form large agglomerates. Unlike the spherical secondary particles in polycrystalline layered cathodes such as LCO, NCM, or NCA where the primary particles are densely packed, in LFP the particles loosely agglomerate as a result of carbon coating applied by the commercial suppliers to improve its electrochemical performance. This, however, makes it nearly impossible to prepare a cohesive FIB lamella to investigate the cross-section. The pristine LATP is visualized in Figure S1 of Supporting Information. Most particles are less than a micron in length. The smaller particles tend to agglomerate but not as much as the LFP CAM. The co-sintering of the cathode and SE material systems necessitates a ball-milling procedure to blend the LATP SE and LFP CAM to form percolating pathways. Figure 1b–d shows the surface morphology of the composites after ball-milling and sintering. The composite sintered at 650 °C (Figure 1b) shows particles with dimensions similar to the individual particles of pristine LFP (≈ 0.5 to 2 μm). A contrast difference can be observed between the two material systems and is demarcated by green dashed lines. Since

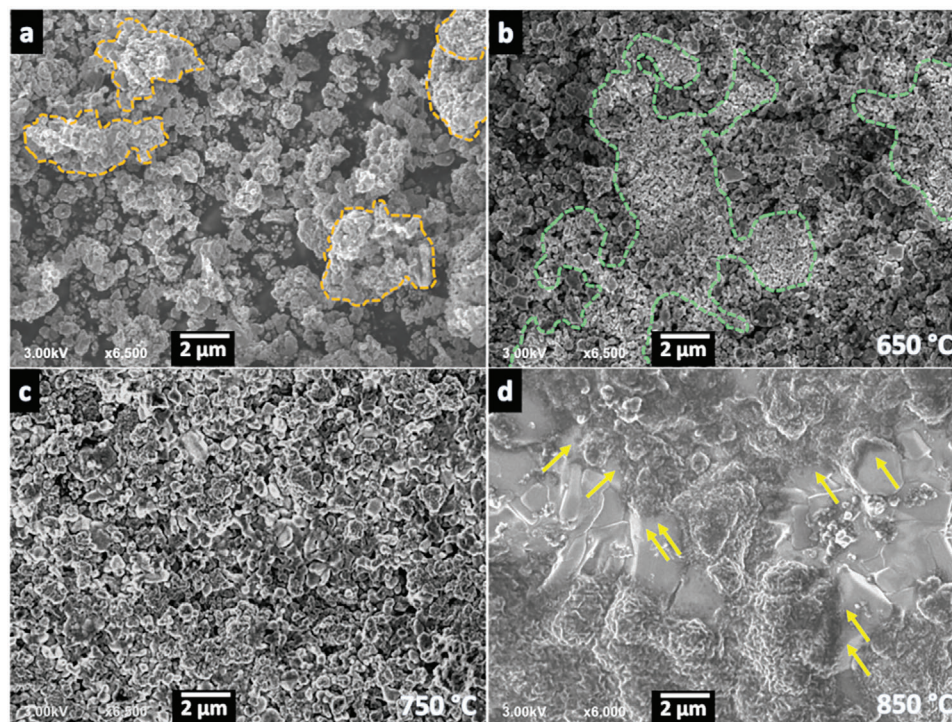


**Figure 1.** SEM micrographs comparing the surface morphology of pristine LFP CAM and LFP-LATP composites. a) Pristine LFP CAM with dashed enclosures (orange) highlighting large agglomerates. LFP-LATP composites co-sintered at b) 650 °C, c) 750 °C, and d) 850 °C. The green dashed delineations in (b) demarcate the two material systems based on contrast differences while the yellow arrows in (d) highlight the cohesive interfaces between the phases.

the image is generated from a combination of secondary and backscattered electrons which primarily offers topological contrast here, we refrain from identifying the phases based on contrast differences.<sup>[23]</sup> Both the dark and light particles still appear loosely packed without sharply defined interfaces between them. The materials tend to cluster and agglomerate as a result of morphological differences and the smaller particle size of LATP.<sup>[24]</sup> The speed of the ball mill influences the rate of agglomeration. Lower speeds result in a slower rate of agglomerate formation while higher speeds tend to cause faster breakdown of particles and quicker agglomerations. Hence, the speed of milling is kept intentionally low at 100 rpm to produce a good blend of materials. Figure 1c shows the composite sintered at 750 °C. The particles have begun to amalgamate and it is hard to differentiate the individual phases using contrast variations. There is a noticeable increase and uniformity in particle dimensions. The composite sintered at 850 °C (Figure 1d) again shows the distinctness of the two material systems with differences in texture and contrast and at this temperature, they appear to form sharply defined interfaces (yellow arrows) with each other. The smooth textured bright contrasted material seems to form well-defined facets while the darkly contrasted material appears grainy yet cohesive.

To elucidate the microstructure of the composites, TEM lamellae were prepared and subjected to STEM investigations. The cross-section of the composites is illustrated with the help of STEM-HAADF and STEM-EDX micrographs as shown in Figure 2. The dark background in between the particles corresponds to the vacuum of the system. Figure 2a shows the cross-section of

the composite sintered at 650 °C. Two regions are highlighted with dashed boxes containing particles of varying form and dimensions. The contrast in HAADF is proportional to both atomic number and thickness.<sup>[25]</sup> Hence, a clear distinction between the material components is non-trivial and so the particles in these regions were subjected to STEM-EDX mapping as shown in Figure 2b,c. In the elemental maps, Fe (blue) represents the LFP particles whereas Ti (red) represents the LATP particles. From these maps, it can be seen that the LFP particles have a range of dimensions. The biggest particle (Region 2, Figure 2c) is undergoing drastic morphological changes. Severe cracking is observed in the bulk while the grain boundaries are disintegrating into smaller particles. However, this might be an outlier as no other large particle was observed with cracks. The LATP particles show more uniformity in dimensions (< 1 μm). Since the EDX maps are unprocessed, the clustering of Ti signals on LATP particles results from variation in the thickness of the particles, i.e., thicker regions generate more X-rays. Figure 2d shows the composite sintered at 750 °C where the two materials systems are starting to amalgamate together and form interfaces beginning with the smaller cathode particles (< 1 μm). The interfaces can be distinguished as sharp boundaries connecting brighter and darker particles (orange arrows). The bright particles correspond to phase(s) related to LFP while the dark particles correspond to phase(s) related to LATP. Compared to 650 °C, the LFP particles (bright) show more uniformity in dimensions and morphology. The vertical dark and bright contrast bands (green arrows) are curtaining artifacts that arise as a result of irregular surface



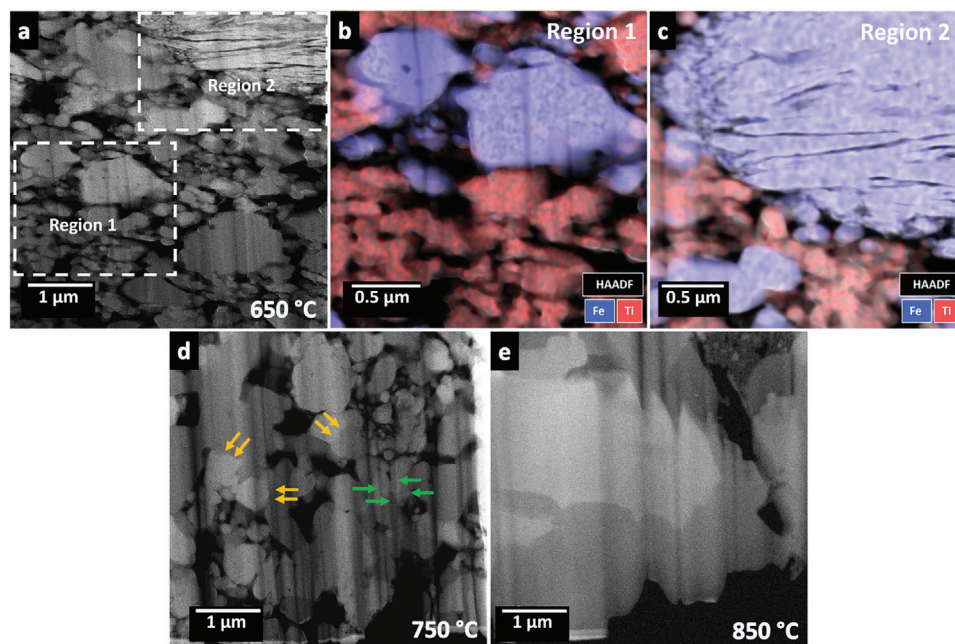


**Figure 2.** Morphology of LFP-LATP CSE composites co-sintered between 650 °C and 850 °C. a) HAADF micrograph of the composite at 650 °C. b,c) STEM-EDX images highlighting the variation in particle dimensions and morphology in (a). d) HAADF micrograph of the composite at 750 °C. The cohesive interfaces are marked with orange arrows. The curtaining artifacts are marked with green arrows. e) HAADF micrograph of the composite at 850 °C.

geometry during FIB milling. To diminish this artifact, the surface of the composite pellet sintered at 850 °C was initially milled at a grazing angle as shown in Figure S2 of Supporting Information. This reduces the surface roughness to a manageable degree while the grazing incidence also reduces  $\text{Ga}^+$  ion implantation on the surface. Figure 2e shows the composite sintered at 850 °C where the large bright particle at the center has formed cohesive interfaces with the darker particles all around its boundary. Thus, between 750 and 850 °C, the larger CAM particles also chemically bond with the SE particles. It is interesting to note that compared to the composite at 650 °C, here the low contrast SE particles also appear to have densified. The densification of phase pure LATP SE without sintering additives takes place at  $\approx 1100$  °C, therefore densification between 750 and 850 °C bears evidence of reactive sintering or in-situ evolution of secondary phases which might act as sinter additives.<sup>[24]</sup>

## 2.2. Evolution of the Atomic Structure of LFP Particles

The microstructural evolution at the atomic scale can offer important insight into the distinct changes that can take place between the bulk and boundary regions of the composites. The changes in LATP SE particles are hard to track via high-resolution STEM on account of the dose ( $< 10^3 \text{ eÅ}^{-2}$ ) acceptable to inhibit beam-induced phase changes. Figures 3 and 4 illustrate the bulk microstructural evolution of LFP particles when co-sintered with LATP solid electrolyte. Figure 3a–c shows the low magnification HAADF micrographs from the pristine LFP CAM and LFP from the composites co-sintered at 750, and 850 °C, respectively. Figure 3c is from the lamella shown in Figure S2b of Supporting Information and therefore the bright and dark fringes

across the image are curtaining artifacts and not a feature of the specimen. Figure 3d–f shows high-resolution micrographs corresponding to regions marked in red boxes in Figure 3a–c. For HRSTEM micrographs, consecutive acquisitions were taken and stacked on top of each other to account for drift and control beam damage. The scale of the stacked data sets was then calibrated to make comparisons with line profiles. The LFP exists in the orthorhombic crystal system and belongs to the spacegroup  $Pnma$ . All HRSTEM images are viewed along the  $[012]$  zone axis as indicated by the FFT inset at the top-right corner in Figure 3d. The atomic structure is visualized in Figure S3a of Supporting Information. Comparing Figure 3 and Figure S3a (Supporting Information), the bright zig-zag planes in the HAADF image consist of Fe atomic columns and are marked by orange arrows. The Li columns are located along the green arrows and generate no contrast in the HAADF image. As visualized in Figure S3a of Supporting Information, the Li atomic columns are flanked on either side by the P atomic columns while the O atoms cluster around the Fe, P, and Li atoms. The distance between the Fe ( $Z = 29$ ) and P ( $Z = 15$ ) plane is  $\approx 1.27 \text{ Å}$  in this projection which should in principle make them distinctly resolvable in the high-resolution HAADF image, however, the reduced signal-to-noise ratio (SNR) to account for beam sensitivity and the oxygen clustering results in spreading of the beam and it appears as if the Fe–P columns are a single feature that connects the adjacent zig-zag columns. A similar phenomenon is observed in other low-dose HRSTEM-HAADF reports of LFP and metal-organic frameworks.<sup>[26–28]</sup> The insets at the bottom-right corner of the HRSTEM images show averaged intensity profiles taken from the middle of the HAADF images marked by the cyan dashed lines. The peaks in the intensity profile correspond to Fe atomic columns while the alternating valleys correspond to Li atomic columns. The peak shoulders

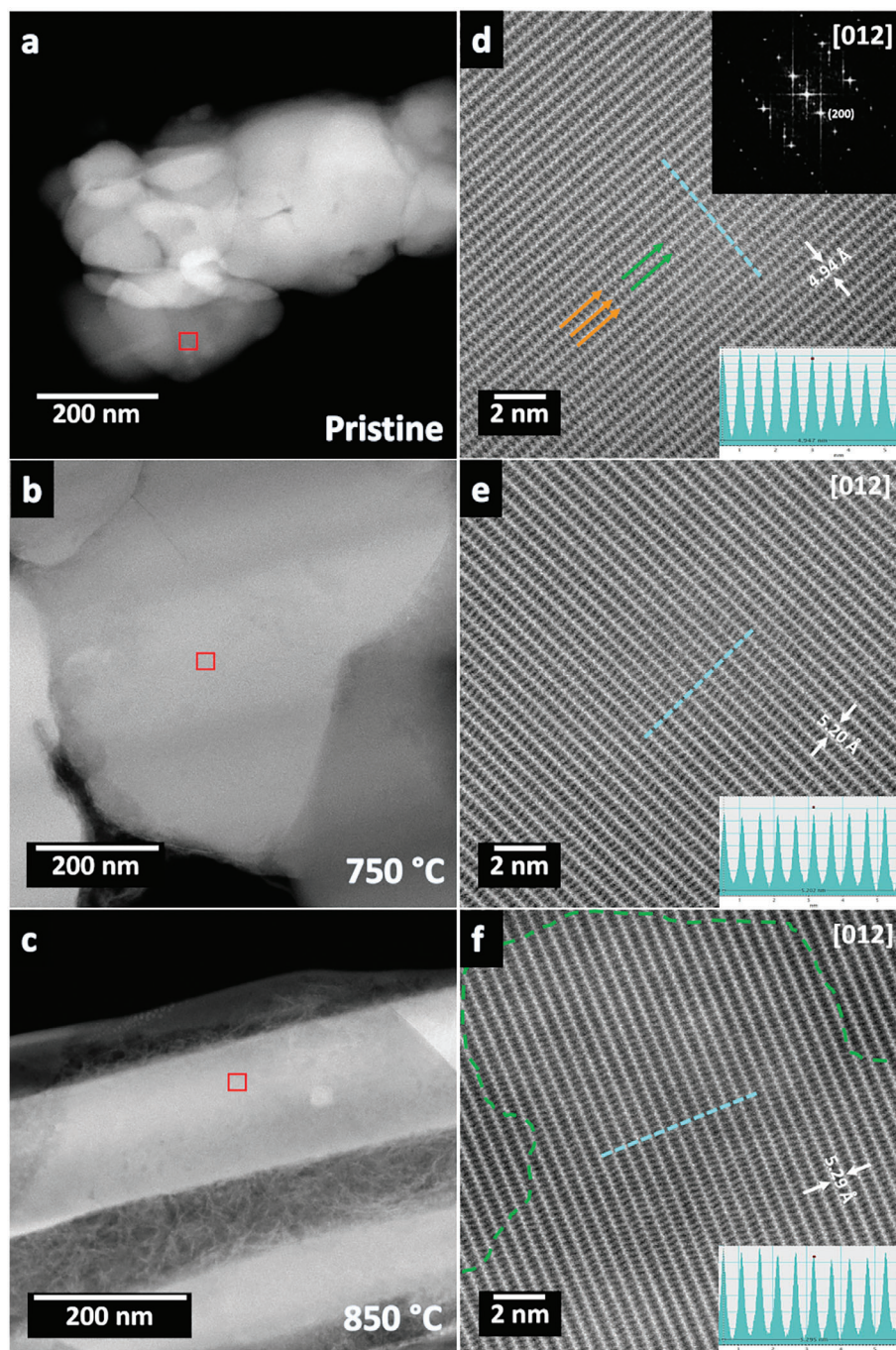


**Figure 3.** Structural stability of LFP particles in the composites with temperature evolution. a–c) Low-magnification HAADF images of pristine LFP, and LFP from composite sintered at 750 °C, and 850 °C, respectively. d–f) HRSTEM-HAADF images from red boxes in (a–c) viewed along the [012] zone axis as shown by the FFT inset at the top-right corner. The bright zig-zag planes (orange arrows) consist of Fe atoms. The lithium atoms are located along (200) planes marked by green arrows. The Fe–P atoms appear as a single feature connecting the zig-zag planes. The insets at the bottom-right corner show averaged intensity profiles from dashed cyan lines. Contrast variation as a result of temperature-induced mass flow is highlighted by the green dashed curve in (f).

correspond to the P and O atomic columns. On comparing the intensity profiles, it is observed that the spacing between the zig-zag Fe planes increases from 4.94 Å in the pristine LFP (Figure 3d) to 5.20 Å in the LFP co-sintered at 750 °C (Figure 3e), and to 5.29 Å in the LFP co-sintered at 850 °C (Figure 3f). This increase in

interplanar spacing could result from  $\text{Fe}_{\text{Li}}$  anti-site defect where Fe atoms occupy Li atomic sites or from Ti/Al diffusion from the solid electrolyte with the temperature rise. The intensity profiles do not indicate the presence of high Z cationic atoms at the Li sites, i.e., there is no noticeable increase in intensity at the



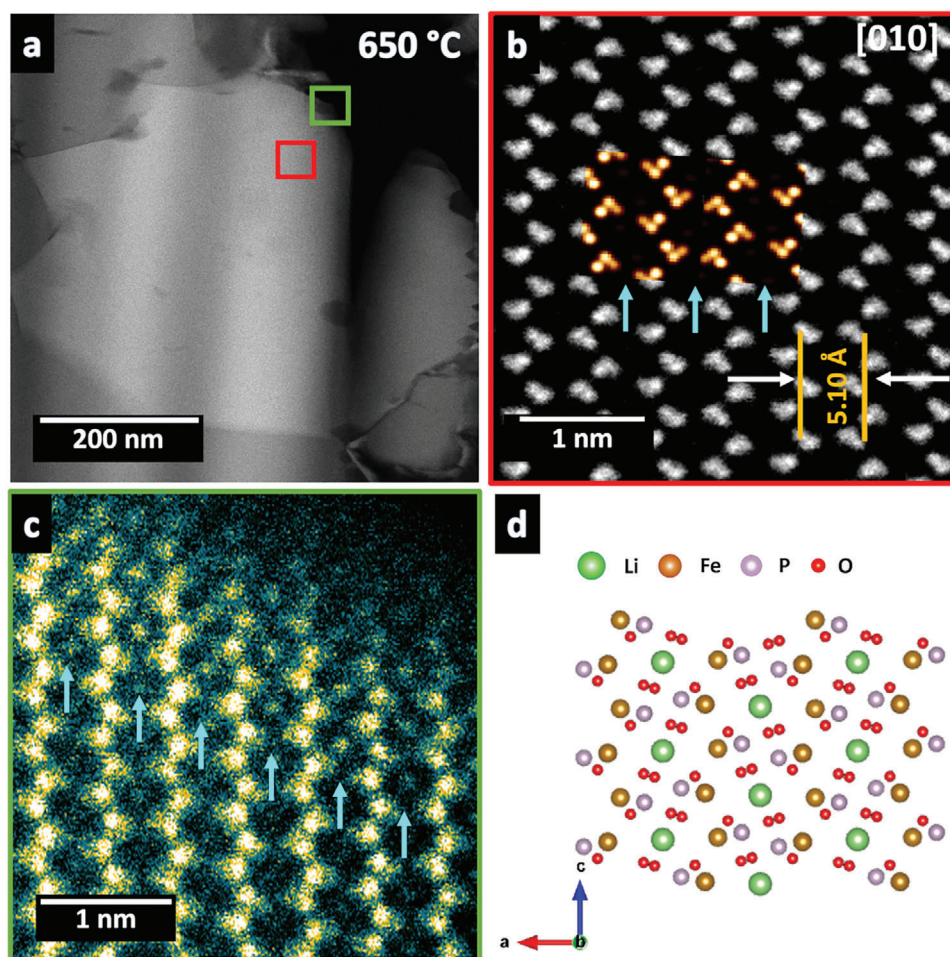


**Figure 4.** Microstructural evolution of LFP in composites co-sintered at 650 °C. a) Low magnification HAADF micrograph of LFP particles. b,c) HRSTEM-HAADF micrograph of the bulk and grain boundary in the [010] zone axis from the red and green boxes in (a). (b) is subjected to background subtraction and (c) is presented in pseudo color to enhance contrast and show  $\text{Fe}_{\text{Li}}$  anti-site defect. d) Visualization of the LFP atomic structure in [010] zone axis with Li (green), Fe (orange), P (purple), and O (red) atoms. The overlaid inset in (b) shows the simulated HAADF image. The antisite defects are formed when Fe (orange) replaces the Li (green) atom. The cyan arrows show the Li rows which are dark in (b) and have bright contrast in (c) indicating  $\text{Fe}_{\text{Li}}$  antisite defect.

valleys between the Fe peaks. The information from HAADF cannot rule out Ti/Al substitution at the Fe site. However, owing to the smaller ionic radii of  $\text{Ti}^{4+}$  (60.5 pm, coordination – 6) and  $\text{Al}^{3+}$  (53.5 pm, coordination – 6) as compared to  $\text{Fe}^{2+}$  (78 pm, coordination – 6) and  $\text{Li}^+$  (76 pm, coordination – 6), it is thought to be difficult for the LFP phase to be doped by Ti/Al.<sup>[29]</sup> The green dashed curve in Figure 3f outlines the contrast variation as a result of temperature-induced mass flow which leads to localized differences in material density within the bulk. The HAADF image is subjected to low-pass filtering and shown in Figure S3b of Supporting Information with pseudo-coloring to distinctly highlight the density variation. The volume changes resulting from these localized effects could also result in variation in interplanar spacing without obvious changes in the phase of the material.

The HAADF micrograph of LFP particles from the composite sintered at 650 °C is shown in Figure 4. The HRSTEM micrographs from the bulk (red box) and grain boundary (green box) are shown in Figure 4b,c in the [010] zone axis. The inset in Figure 4b is a simulated HRSTEM-HAADF micrograph of LFP

in the [010] zone axis which agrees well with the experimental image. Figure 4c is presented in pseudo-color to enhance the contrast in the Li columns. The atomic structure of LFP is visualized in the same zone axis in Figure 4d. The cations  $\text{Li}^+$  (green) and  $\text{Fe}^{2+}$  (orange) occupy the octahedral M1 and M2 sites, respectively, while the P atoms occupy the tetrahedral site. In this projection as well, the distance between the Fe–P plane is  $\approx 1.27$  Å but as mentioned above, the reduced SNR and the arrangement of atoms make it challenging to resolve the atomic columns distinctly in the experimental HAADF images (Figure 4b,c). As such the Fe–P columns appear as triangle-shaped features consistent with other reports.<sup>[26,27]</sup> The distance between the Fe zigzag planes is 5.10 Å and is in between that of the pristine sample and LFP co-sintered at 750 °C. On comparing Figure 4b,c (cyan arrows) it is seen that the bulk maintains its structural stability while the grain boundary shows clear evidence of cation disorder ( $\text{Fe}^{2+}$  at the M1 site). It is quite remarkable that the cation ordering is limited to a few nms from the GB at 650 °C as no significant difference in lattice spacing is observed between the

bulk and GB. On analyzing Figures 3 and 4 it is seen that the LFP particles maintain their bulk structural stability (no drastic phase transformation) with the evolution of temperature from 650 °C to 850 °C. At 650 °C, the  $\text{Fe}_{\text{Li}}$  anti-site defect is present at the grain boundaries. The rise in temperature results in an increase in interplanar spacing without the noticeable presence of cation ordering. It should be noted here that HRSTEM analysis is limited to particles in high symmetry zone axis and hence further investigations with complementary techniques are required to establish their microstructural stability/evolution in the composites.

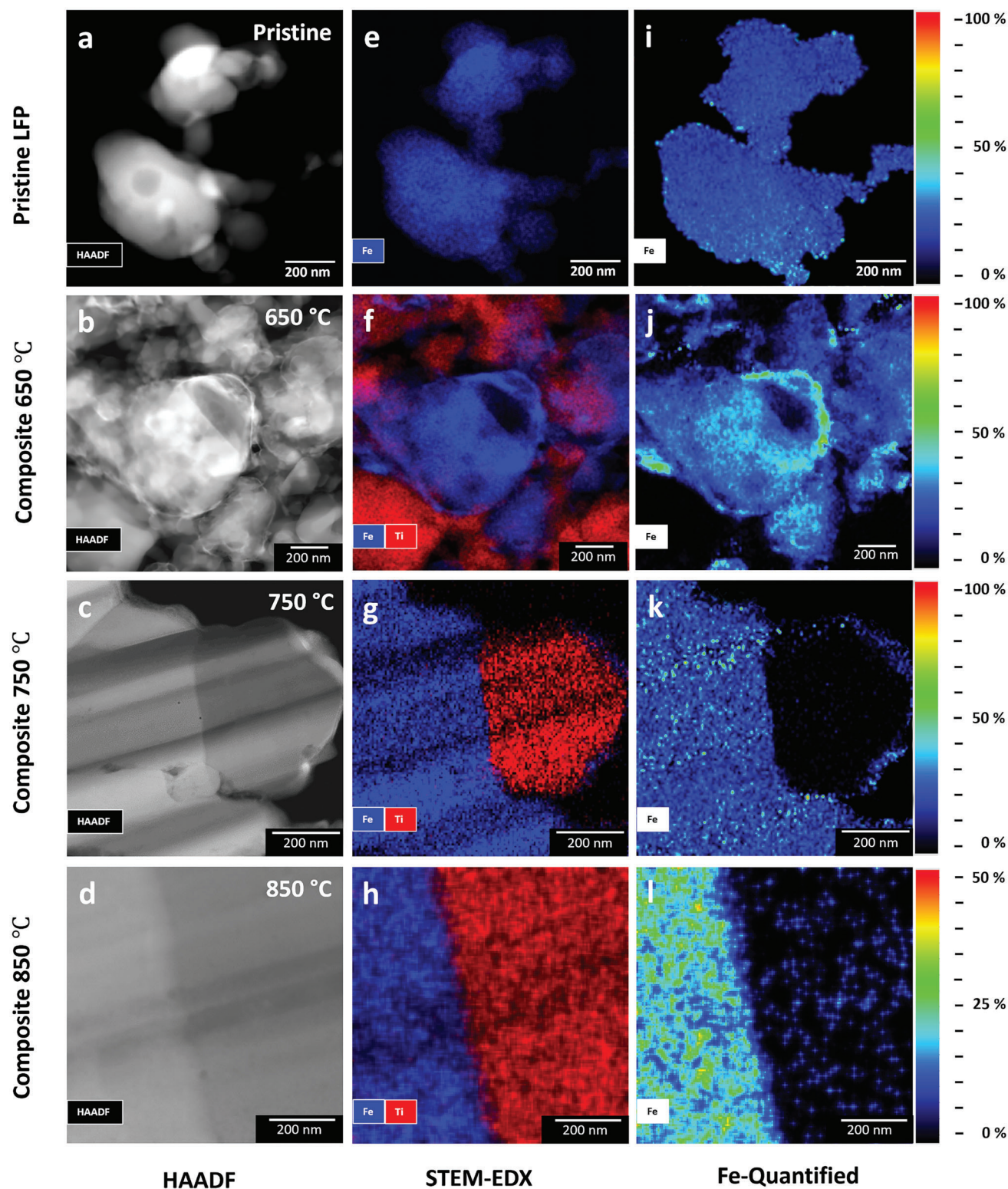
### 2.3. Composition and Phase Evolution at the CSE Interfaces

The chemical evolution taking place in the CSE co-sintered composites is compared with the pristine LFP material utilizing STEM-EDX mapping in Figure 5. Figure 5a–d consists of HAADF micrographs of pristine LFP and LFP-LATP composites co-sintered at 650, 750, and 850 °C, respectively. The elemental maps in Figure 5e–h and the quantified Fe maps in 5i–l correspond to Figure 5a–d. The Fe maps are quantified using the Cliff-Lorimer ratio method but cannot account for lithium (due to instrument limitations) and hence do not represent absolute compositions but should suffice to compare the relative Fe atomic percentage compositions between the composites. The pristine LFP (Figure 5a,e,i) shows that Fe is homogeneously distributed throughout the particles. Contrast changes are observed in the HAADF image (Figure 5a) at the center of the particle (dark circular region) and at grain overlaps, however, these are not reflected in the quantified Fe map (Figure 5i) and consequently only related to the changes in the thickness of the material. In the composite sintered at 650 °C, the particles show varying amounts of contrast variations (Figure 5b). From the Fe–Ti combined elemental map (Figure 5f) and Fe quantified map (Figure 5j), the central particle shows one large area and several smaller areas deficient in Fe while at the same time enriched with Fe at the grain boundaries. The Fe enrichment at the grain boundary is compositionally nearly twice ( $\approx 60\%$ ) as much as the bulk regions ( $\approx 30\%$ ). This bears further evidence that Fe occupies the M1 Li sites as was previously observed in the high-resolution micrographs as it moves from the bulk to the surface. Additionally, it is observed that the grain boundary Fe segregation is inhomogeneous as it is only present on a couple of facets of the particle. The composite sintered at 750 °C shows a clear interface between the LFP and LATP particles as shown in Figure 5c,g. It is also observed here that the LATP particle boundary exposed to the vacuum appears brighter and on comparing with the elemental map (Figure 5g) and quantified map (Figure 5k) it is seen that there is significant segregation of Fe along the boundary of LATP particle. Thus in addition to the cohesive interface between the two components, we observe here the interdiffusion of Fe along the LATP particle boundaries. At 850 °C, the material system is extremely susceptible to beam-induced damage at high magnifications as a result of higher electron dose impinging on the specimen as shown in Figure S4 of Supporting Information. Therefore, a spectrum imaging dataset was taken over a large field of view as shown in Figure S5 of Supporting Information. As the total number of pixels was kept constant (512×512), the

increased field of view resulted in a reduced sampling size (undersample). These steps were incorporated to effectively spread the total electron dose and prevent beam-induced changes on the specimen during EDX data acquisition. Figure 5d,h,l are EDX maps cropped from the original dataset and correspond to the interface shown in the red box in Figure S5 (Supporting Information). The elemental map in Figure 5h again shows a smooth interface between the CAM and SE particles. Fe diffusion into the SE particle is observed in the quantified map as shown in Figure 5l. This map has been rescaled to increase the contrast and distinctly highlight the Fe signals in the SE phase which is  $\approx 10\%$ . The dark and bright contrast bands that run across the images in Figure 5c,g,d,h correspond to the curtaining effect as discussed previously. Additionally, in the original dataset in Figure S5 (Supporting Information), we observe a dark phase that separates the upper and lower regions (pink-dashed lines). The elemental maps indicate that this region consists of mostly C species. It is known that carbon coatings on LFP decompose at higher temperatures ( $> 800\text{ °C}$ ) forming gases ( $\text{CO}/\text{CO}_2$ ) that produce large pores and destroy the microstructure of LFP.<sup>[30]</sup> In our case, we suspect a non-homogenous decomposition of carbon in our sample. Furthermore, the Ti and Al composition maps corresponding to the composite regions shown in Figure 5b–d are shown in Figure S6 of Supporting Information. It is seen here that Ti and Al show  $\approx 5\text{--}10\%$  diffusion into the LFP only at the very high temperature of 850 °C possibly replacing the Fe sites in LFP.

To further illustrate the phase evolution that has occurred in the composite co-sintered at 850 °C, the TEM lamella in Figure 2c was subjected to the ACOM-TEM phase mapping technique as shown in Figure 6. The HAADF-STEM micrograph in Figure 6a shows an overview of the lamella subjected to phase analysis. Figure 6b is an exemplary phase map that was generated using the ACOM-TEM technique from the region marked in the red box in (a). At 850 °C the dominant phase present in the region is still the orthorhombic LFP ( $\text{LiFePO}_4$ ,  $Pnma$  spacegroup, blue). The trigonal LATP ( $\text{Li}_{1.3}\text{Al}_{0.3}\text{Ti}_{1.7}(\text{PO}_4)_3$ ,  $R\bar{3}c$  spacegroup, red) solid electrolyte has a negligible composition ( $< 0.5\%$ ) in the mapped area. Instead, two new orthorhombic phases are observed having different symmetries ( $Pbca$ : yellow and  $Pbcn$ : orange). These phases are indexed with  $\text{Li}_2\text{FeTi}(\text{PO}_4)_3$  CIF files which are considered as phase equivalent to the new phases as the exact composition of the new phases depends on the value of  $x$  (Fe substitution) in the general formula  $\text{Li}_{1.3+x}\text{Al}_{0.3}\text{Fe}_x\text{Ti}_{1.7-x}(\text{PO}_4)_3$ . The interplay of Fe substitution with temperature rise and its effect on the electrochemical performance of the composite is discussed in the ensuing sub-section. The particle containing an interface between the two new phases is marked in a green box in Figure 6 and is magnified and illustrated as a HAADF image in Figure 6c. The phase map suggests that three orthorhombic phases co-exist in the particle (green box in Figure 6b) signifying that the composition at the phase boundary greatly varies. This is reflected in the speckled phase pattern along the phase boundary indicating that the phase-matching algorithm arrives at nearly equivalent solutions in this region. Figure 6d shows an HRSTEM-HAADF micrograph of the bright region marked by the orange box in Figure 6c. A representative region from the HRSTEM image is magnified, and its background is subtracted and displayed in the inset. This inset is







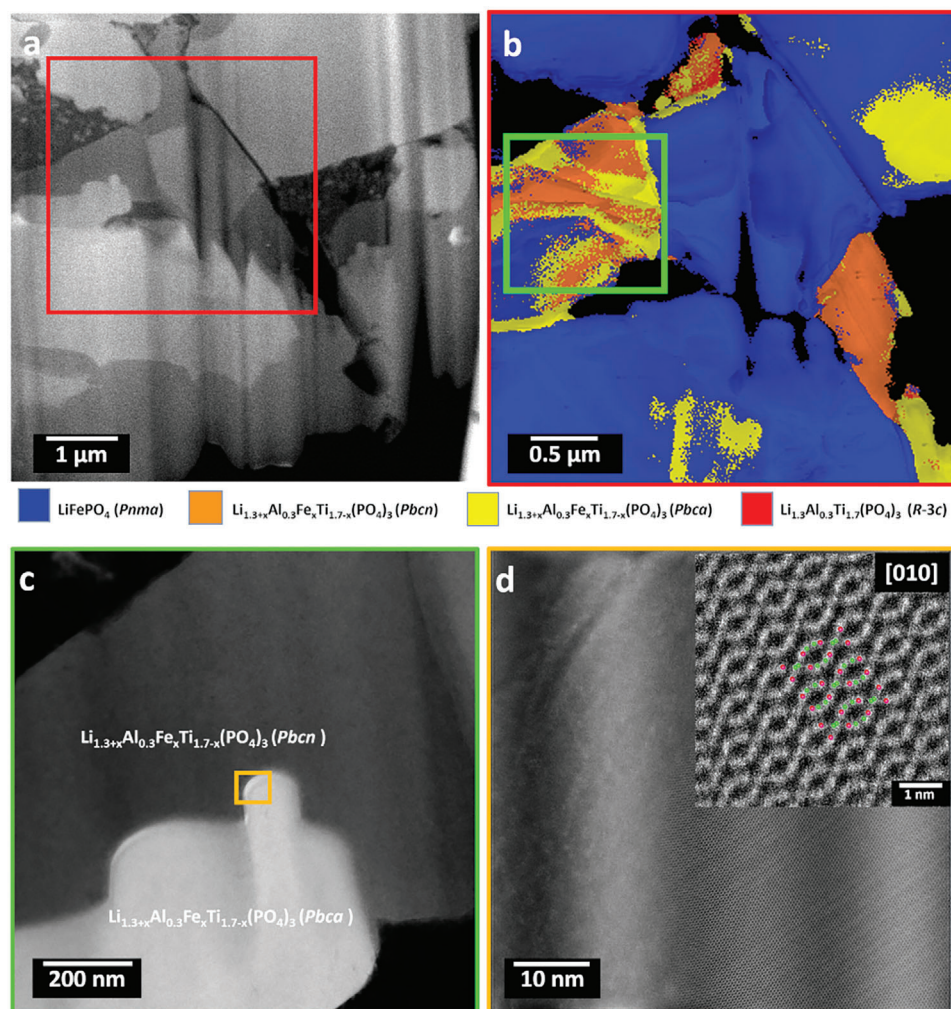


**Figure 6.** Phase evolution in LFP-LATP CSE composites co-sintered at 850 °C. a) Overview HAADF-STEM micrograph showing intimate interfaces between bright and dark contrasting grains. b) Phase map from a region marked in the red box in (a). c) High magnification HAADF micrograph at the interface region marked with a green box in (b). d) HRSTEM micrograph of interface marked in the yellow box in (c). The inset shows a background subtracted magnified view overlaid with Fe/Ti (magenta), and P (green) atoms to enhance visualization in the [010] zone axis of the Pbcn phase. At 850 °C, the trigonal LATP (red) has transformed into two orthorhombic  $\text{Li}_{1.3+x}\text{Al}_{0.3}\text{Fe}_x\text{Ti}_{1.7-x}(\text{PO}_4)_3$  phases (Pbcn and Pbca spacegroup). The index shows the color code of phases present in the composite.

overlaid with the atomic arrangement of  $\text{Li}_2\text{FeTi}(\text{PO}_4)_3$  (Pbca spacegroup) viewed in the [010] zone axis showing only the Fe/Ti (magenta) and P (green) atoms to simplify the visualization of the complicated structure. As the Pbcn phase was more susceptible to beam damage at the same dose during atomic resolution imaging, it could not be effectively resolved.

Comparing Figure 5 and Figure 6, it is observed that with the evolution of temperature from 650 °C to 750 °C, Fe segregates within the LFP phase and also migrates into the LATP solid electrolyte across their grain boundaries. Intimate interfaces between the cathode and solid electrolyte already start to appear at 750 °C. Between 750 and 850 °C, a large portion of the trigonal R-3c phase in the solid electrolyte component transforms to orthorhombic Pbca or Pbcn spacegroups as an increasing amount of Fe interdiffuses into its bulk. The phase map also suggests that LFP CAM mostly remains intact with minor phase variations observed at its grain boundaries and bulk which reflect variations in lattice

spacings. The stability of the structure arises from the robustness of  $(\text{PO}_4)^{3-}$  polyanions while the minor variations may result from the diffusion of Ti and Al into the CAM at this temperature. By increasing the substitution of  $\text{Ti}^{4+}$  and  $\text{Al}^{3+}$  by  $\text{Fe}^{2+}$ , the crystal structure of LATP however, changes from trigonal to orthorhombic phases. The thermodynamic and crystallographic reasons for this behavior have not yet been justified but may correlate with the size of the cations. This is also detected by X-ray powder diffraction of the composites after co-sintering as shown in Figure S7 of Supporting Information. The position and intensities of reflexes in the olivine phase of the LFP CAM are maintained without significant variations even after co-sintering at 850 °C, whereas the reflex intensities of LATP (R-3c) decreased with increasing sintering temperature. For sintering temperatures of  $T > 750$  °C, new crystalline phases can be detected that are assigned to orthorhombic  $\text{Li}_{1.3+x}\text{Al}_{0.3}\text{Fe}_x\text{Ti}_{1.7-x}(\text{PO}_4)_3$  ( $x > 0.3$ ). This indicates the substitution of Fe into the LATP bulk.

## 2.4. Fe Interdiffusion and Electrochemical Modulation at Elevated Temperatures

As a CAM, LFP ( $\text{LiFePO}_4$ ) shows excellent thermal stability as compared to its energy-dense competitors, the layered  $\text{LiCoO}_2$  and its variants the NCA/NCM. We previously investigated the thermal instability of NCM-LATP co-sintered composites wherein the microstructural evolution of the layered cathode between 550–650 °C was also examined in detail.<sup>[20,21]</sup> In this case, with an increase in temperature the solid electrolyte LATP acts as a sink for Li, de-lithiating the NCM. Excess loss of lithium leads to irreversible phase changes from layered to spinel to cubic. Moreover, since the oxygen atoms are weakly bound, the thermal driving force leads to O vacancy condensation at dislocation cores which ultimately leads to crack formation to accommodate the volumetric and compositional changes. In the LFP, however, both  $\text{FeO}_6$  octahedra and  $\text{PO}_4$  tetrahedra provide structural support for the crystal system, thus even when LATP acts as a sink for Li, delithiation does not involve a total structural collapse during heat treatment. When LFP particles transform to  $\text{FePO}_4$ , the space-group remains unchanged even though the particles experience a volume change of  $\approx 6.81\%$ .<sup>[31]</sup> Moreover, unlike NCM, the oxygen is strongly bonded with phosphorous forming covalent bonds in  $(\text{PO}_4)^{3-}$  polyanionic clusters. Nevertheless, the same framework that gives the crystal structure its stability also presents an obstacle to electronic conductivity. The  $\text{FeO}_6$  octahedra are corner-shared making the distance between the neighboring Fe atoms greater than 4 Å. For conductive oxides, the M-M (metal to metal) distance should be  $< 3$  Å.<sup>[32]</sup> Consequently, the electronic conductivity of the  $\text{LiFePO}_4$  is in order of  $10^{-9} \text{ S cm}^{-1}$  which is similar to the solid electrolyte LATP making LFP essentially an insulator.<sup>[33]</sup> Thus the performance advantage provided by the fast Li diffusion pathway resulting from the similarity in the crystal structure of the two phases (LFP and  $\text{FePO}_4$ ) is hindered by its low electronic conductivity. Additionally, unlike the 2-D diffusion pathways in NCM, the Li diffusion in LFP is restricted to a single dimension along the *b*-axis.<sup>[13,31]</sup> In LFP nanoparticles, it is reported that annealing in an oxygen-rich atmosphere above 200 °C results in Fe extrusion and redistribution in M2 and M1 sites which leads to the formation of complex structures of the type  $\text{LiFe}_{1-y}\text{PO}_4$ .<sup>[34,35]</sup> On the other hand, LFP remains stable when annealed in an inert atmosphere up to a temperature of 775 °C.<sup>[22]</sup> In our case, co-sintering was carried out under  $\text{N}_2$  flow over the entire temperature range from 650 °C to 850 °C. At 650 °C, Fe extrusion (Figure 5b,f,j) as well as redistribution of M2  $\text{Fe}^{2+}$  into the M1  $\text{Li}^+$  sites ( $\text{Fe}_{\text{Li}}$  anti-site defect, Figure 4c) is observed providing evidence for Fe diffusion from the bulk to the surface regions. The  $\text{Fe}_{\text{Li}}$  anti-site defect presents an obstacle to lithium diffusion which would degrade the electrochemical performance.<sup>[31,36]</sup> The  $\text{Li}^+$  cations (M1 site) have a shorter distance between each other owing to their edge-shared octahedra as opposed to the corner-shared octahedra of  $\text{Fe}^{2+}$  cations (M2 site).  $\text{Fe}_{\text{Li}}$  anti-site defects will cause additional repulsion between the cations due to high-valent and slighter larger Fe occupying the M1 site and at sufficiently high aggregations will expand the unit cell along the *a* and *c*-axes with the *c*-axis experiencing the most deviation.<sup>[37]</sup> Since the Fe planes in Figure 3 lie perpendicular to the *a*-axis (Figure S3a in Supporting Information), this fits well with the increase in interplanar spacing that we observe between them. The Li/Fe or-

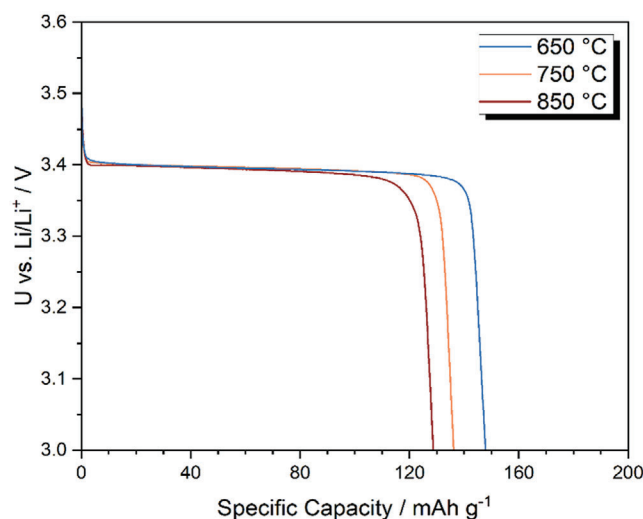


**Figure 7.** Discharge profile (0.1 C) of tape-casted LFP-LATP composites after co-sintering between 650 – 850 °C. The porous microstructure of the cathodes is infiltrated with liquid LP40 electrolyte to enhance interfacial contact and increase ionic conductivity within the sintered composite cathode.

dering, however, is orientation-dependent, and their aggregation is confined along the [010] direction (*b*-axis).<sup>[38]</sup> This explains the apparent absence of antisite defects at higher temperatures when viewed in the [012] direction in Figure 3. Thus, starting at 650 °C, some of the cathode particles in our composite system exhibit complex behavior related to Fe segregation.

To improve the electronic conductivity of the bare LFP, commercial suppliers typically coat  $\text{LiFePO}_4$  with carbon ensuring that these CAMs reach capacities close to their theoretical capacity of 170  $\text{mAh g}^{-1}$ .<sup>[39]</sup> It is speculated that admixing carbon precursors during the synthesis process suppresses LFP particle growth and hence shortens the diffusion path of Li-ions.<sup>[40,41]</sup> In addition, carbon could also act as a reducing agent during the synthesis preventing the oxidation of  $\text{Fe}^{2+}$  to  $\text{Fe}^{3+}$ .<sup>[42]</sup> However, our results indicate that during the co-sintering process, the carbon present as coatings on the LFP cathode is insufficient to suppress the growth of LFP at elevated temperatures (Figure 2). This increase in dimension is suspected to hinder the Li diffusion kinetics within the LFP during cycling.<sup>[22]</sup> Moreover, it is also observed that some amount of carbon phase separates within the composites at 850 °C. To evaluate their electrochemical performance, the co-sintered LFP-LATP composites were tape-casted and subjected to cycling as shown in Figure 7 and Figure S8 of Supporting Information. The potential profile of the sintered composite tapes shows a flat discharge potential at 3.40 V versus  $\text{Li/Li}^+$ , which is typical for  $\text{LiFePO}_4$ . The specific capacities decrease with the increase in the sintering temperature of the composites. The result shows discharge capacities of 148  $\text{mAh g}^{-1}$  at 0.1C after co-sintering at 650 °C. At 750 °C, the capacity decreases to 137  $\text{mAh g}^{-1}$ , and at 850 °C, the capacity further reduces to 130  $\text{mAh g}^{-1}$ . The lower capacities could be caused by antisite defects, particle growth, or the decomposition of the carbon coating.<sup>[31,43]</sup> All effects enhance with increasing sintering temperature and can lead to reduced  $\text{Li}^+$  and electron transport within the active material. It should also be noted that the higher capacity at 650 °C



may result from better wetting of the porous composite by the liquid electrolyte employed in addition to having smaller particles. The capacities reported in the literature for various carbon-coated LFPs range between 120–165 mAh g<sup>-1</sup> at 0.1 C.<sup>[39]</sup> The capacities reported in our study lie within this range although the utilization of LATP SE does not provide a significant improvement. Nevertheless, the results show that the CSE composites remain electrochemically active even after co-sintering at higher temperatures. More details on the electrochemical performance are given in a forthcoming paper. The acceptable co-sintering temperature should be limited to  $T \approx 750^\circ\text{C}$  to obtain a reasonably competent discharge capacity while avoiding the negative impact of particle growth, carbon decomposition, and phase transformations at higher temperatures.

On the one hand, co-sintering all-phosphate CSE composites (LFP-LATP) in an oxygen atmosphere between 500–900 °C results in a major portion phase transforming to form  $\text{Li}_3\text{Fe}_2(\text{PO}_4)_3$ .<sup>[17]</sup>  $\text{Li}_3\text{Fe}_2(\text{PO}_4)_3$  shows polymorphic behavior and can exist in monoclinic ( $P2_1/n$  spacegroup), as well as orthorhombic phases ( $Pbcn$  spacegroup), and their formation is temperature dependent. The monoclinic phase forms at lower temperatures ( $\approx 50^\circ\text{C}$ ) while the orthorhombic at higher temperatures (300–550 °C) upon oxidation of LFP.<sup>[34,41,44]</sup> On the other hand, co-sintering LFP-LATP in an inert atmosphere ( $\text{N}_2/\text{Ar}$ ) will prevent  $\text{Fe}^{2+/3+}$  oxidation or co-sintering in slightly reducing atmosphere ( $\text{H}_2$ ) will even reduce any remaining  $\text{Fe}^{3+}$  impurities. Sintering standalone trigonal LATP in an inert (Ar) atmosphere up to 775 °C has been shown to result in partial phase transformations to orthorhombic LATP while co-sintering with LFP results in the formation of  $\text{Li}_{3-x}\text{Fe}_{2-x-y}\text{Ti}_x\text{Al}_y(\text{PO}_4)_3$  ( $0 \leq x+y \leq 2$ ).<sup>[22]</sup> Gellert et al., (2018) identified four phases in LFP-LATP co-sintered at 700 °C in an inert atmosphere using back-scattered electron images and SEM-EDX.<sup>[16]</sup> They suggest that the LATP remains intact while the cathode LFP transforms to non-stoichiometric  $\text{LiFe}_{1-x}\text{PO}_4$ . Upon increasing the temperature to 800 °C a new ortho-phosphate  $\text{Li}_{1+x}\text{Fe}_x\text{Ti}_{2-x}(\text{PO}_4)_3$  is formed. In our study, since the co-sintering is carried out in a flowing  $\text{N}_2$  atmosphere, the formation of  $\text{Li}_3\text{Fe}_2(\text{PO}_4)_3$  is successfully prevented. Nevertheless, the interdiffusion of Fe into the solid electrolyte (Figure 5c,g,k) accelerates the formation of orthorhombic LATP phase(s) as almost all the trigonal phase is consumed at 850 °C (Figure 6). More interestingly, the Fe occupation of the Ti site in LATP is inhomogeneous leading to the existence of orthorhombic solid electrolyte phases with two different spacegroups; *Pbca* and *Pbcn*. It is known from the literature that NASICON  $\text{Li}_{1+x}\text{Fe}_x\text{Ti}_{2-x}(\text{PO}_4)_3$  exists in three different crystallographic phases depending on the amount of Fe substituting at the Ti atomic sites.<sup>[45]</sup> If the substitution is less than or equal to 0.6 per unit formula ( $x \leq 0.6$ ), the material remains in the trigonal *R3c* spacegroup. A substitution between 0.7 and 1.0 ( $0.6 < x \leq 1.0$ ) per unit formula results in the formation of the *Pbca* spacegroup and above 1.0 ( $x > 1.0$ ) the *Pbcn* phase is formed. The *Pbca* and *Pbcn* diffractograms are quite similar since the only difference between their lattice is the doubling of the *c* vector for the former phase. The *Pbca* phase also has greater density when compared to the *Pbcn* phase. The HAADF in Figure 6c shows that the phase boundary is brighter and is indexed mostly in the *Pbca* spacegroup in Figure 6b. In addition, the HRSTEM micrograph (Figure 6d) gives a direct image of the atomic arrangement at the

bright region corresponding to the *Pbca* phase viewed in the [010] zone axis. Thus, it is concluded that there is a gradient in Fe diffusion into the solid electrolyte which results in the co-existence of the two solid electrolyte orthorhombic phases when co-sintering to 850 °C. The new phases have Li-ion conductivities at least two orders of magnitude lower than the trigonal phase.<sup>[46]</sup>

On comparing with the oxide-phosphate CSE composites (NCM-LATP), all phosphate composites of LFP-LATP offer better thermal stability (550 °C vs 750 °C) during co-sintering as they can form intimate chemical interfaces without CAM decomposition and disintegration in the form of electrochemically inert phase transitions and cracks. These interfaces, however, result from the diffusion of Fe from CAM into SE and at very high temperatures ( $> 800^\circ\text{C}$ ) leading to the formation of new solid electrolyte phases which have different electrochemical properties as compared to the starting materials. Moreover, increases in particle dimensions and decomposition of carbon also take place at this temperature which negatively impacts the discharge capacity. Thus, the co-sintering temperature in a conventional sintering set-up should be limited to  $\approx 750^\circ\text{C}$  since at this temperature we observe the cohesive interfaces with reasonable particle dimensions and without any carbon degradation.

### 3. Conclusion

In this study, the microstructural evolution that accompanies the high-temperature sintering of all-phosphate CSE LFP-LATP composite is systematically examined using advanced STEM techniques. HRSTEM of the LFP particles from the composites shows that they are fairly stable between 650 and 850 °C. At 650 °C, Fe moves from the bulk to the surface regions leading to  $\text{Fe}_{\text{Li}}$  anti-site defects within the LFP CAM that block the Li-diffusion pathway. At 750 °C, STEM-EDX elemental mapping shows that the Fe interdiffuses into the LATP from the particle surfaces. The two material systems also start forming cohesive interfaces at this temperature as evidenced by low-magnification HAADF micrographs and EDX maps. At 850 °C, the HAADF micrographs show that the LFP particles increase in dimensions while the HRSTEM and phase maps show that they remain structurally stable with only a marginal increase in lattice spacing with Ti/Al interdiffusion. On the solid electrolyte side, the trigonal LATP undergoes a complete phase transformation into two new orthorhombic phases with continuous interdiffusion of Fe. The formation of these new phases depends on the amount of Fe substitution at the Ti atomic sites of the solid electrolyte. The orthorhombic phases offer lower ionic conductivity as compared to the trigonal LATP phase, however, their mixed conductivity can be exploited by controlling their composition. Due to the above effects, the electrochemical performance of the composites reduces with increasing sintering temperature even with the formation of cohesive interfaces. The insight obtained in this work confirms that cohesive interfaces can be synthesized using established sintering technologies by employing cathode and electrode components having a similar anionic framework. To overcome the ion-conductivity bottleneck, the temperature should be limited to  $\approx 750^\circ\text{C}$  for LFP-LATP composites. Further improvements should consider alternative sintering technologies such as cold sintering to achieve the dense-cohesive interfaces without introducing additional phases

or particle growth to manufacture CSE composites from established battery components.

## 4. Experimental Section

**Synthesis of LFP-LATP CSE Composite:** The solid electrolyte,  $\text{Li}_{1.3}\text{Al}_{0.3}\text{Ti}_{1.7}(\text{PO}_4)_3$  (LATP) was prepared by sol-gel synthesis and calcined at 700 °C in air.<sup>[24]</sup> The particle size was reduced to  $d_{50} < 1.0 \mu\text{m}$  by intensive grinding at 1000 rpm in ethanol. The solvent was removed and the powder was mortared. Commercial  $\text{LiFePO}_4$  (Life Power PA30) from Clariant was used as cathode active material (CAM). The SE and CAM were mixed in a 1:1 weight ratio to form the LFP-LATP composites. For this purpose, the powders were suspended in ethanol and milled at 100 rpm for 30 min (Pulverisette 7 Fritsch GmbH). Under reduced pressure, the solvent was removed and the powder was mortared. Subsequently, the powder was pressed at 5 kN to form cylindrical pellets with a diameter of 8 mm. The pellets were sintered on dense  $\text{Al}_2\text{O}_3$  substrates under flowing  $\text{N}_2$  ( $2 \text{ l min}^{-1}$ ). The samples were then heated at  $3 \text{ K min}^{-1}$  to 650–850 °C with a dwell time of 30 min.

**Tape-Casting and Electrochemical Cell Tests:** LATP and LFP powders were mixed with graphite, binders, plasticizers, and dispersants in MEK/EtOH to produce a homogeneous slurry. The slurry was tape-casted using a doctor-blade process with a slit width of 300  $\mu\text{m}$ . Tapes have an active material loading of  $12.3 \text{ mg cm}^{-2} / 2.0 \text{ mAh cm}^{-2}$ . Round samples with a diameter of 18 mm were punched out of the green tape. The samples were debonded at 400 °C and co-sintered at 650–850 °C under flowing  $\text{N}_2$  ( $2 \text{ l min}^{-1}$ ). To improve the electrical contact with the current collector, the sintered composite cathode was sputtered on one side with Au. For electrochemical cell tests, half-cells with lithium metal anode, Whatman glass fiber, and co-sintered LFP-LATP tapes were assembled. The separator and co-sintered composite were infiltrated with liquid LP40 electrolyte. The cells were allowed to rest for 24 h after assembly. The electrochemical tests were performed at 45 °C using a Biologic VMP 3 within a potential range of 3.5 to 2.0 V.

**STEM Sample Preparation:** Focused-ion beam lamella preparation was carried out using a JEOL JIB-4601F dual beam FIB system operating between 1–30 kV for both the electron beam and  $\text{Ga}^+$  ion beam. The surface of the pellet was initially protected from beam-induced damage by coating a thin protective layer of platinum with a thickness of  $\approx 200 \text{ nm}$  with a Leica EM ACE600 Sputter coater. This was followed by  $\approx 4 \mu\text{m}$  thick tungsten layer deposition using the  $\text{Ga}^+$  ion beam at the region of interest (ROI) inside the SEM. The thick lamella produced by milling the ROI was then transferred to an Omni-probe TEM Cu grid using a micro-manipulator needle. A cross-sectional STEM lamella was produced by first milling down to 700 nm with a 30 kV  $\text{Ga}^+$  ion beam and then to 400 nm with a 10 kV beam and finally to 100 nm with a 5 kV beam. Lastly, the cross-section was polished in a Fischione NanoMill 1040 with a 500 eV  $\text{Ar}^+$  ion beam.

**Material Characterization:** The SEM characterization was done using the dual beam JEOL JIB-4601F system. A JEOL JEM-2200 FS STEM was used for HAADF (High-Angle Annular Dark Field) characterization. The STEM was equipped with two spherical aberration correctors and was operated at 200 kV with a 21.3 mrad convergence angle. The beam current was varied between  $\approx 6 \text{ pA}$  and  $\approx 24 \text{ pA}$ . The HAADF images were taken by setting the inner angle of the annular dark field detector to 70 mrad. During HRSTEM acquisition, the  $\text{e}^-$  beam dose was varied between  $10^4$ – $10^5 \text{ e}\text{\AA}^{-2}$  which corresponds to low and medium-dose STEM microscopy, respectively.<sup>[47]</sup> The influence of the beam damage was further reduced by collecting and aligning several individual fast acquisitions by the Smart Align script.<sup>[48]</sup> Image analysis (including intensity profiles) was carried out using the software package Gatan Digital Micrograph. All EDX maps were taken with a frame size of  $512 \times 512$  pixels. A JEOL JEM-3010 TEM equipped with a Nanomegas ASTAR system was used to collect the diffraction data required to generate the phase maps with the ACOM-TEM method. This microscope was operated at 300 kV. To minimize the influence of dynamic scattering, the electron beam was processed at 0.6°.

The final probe size was  $\approx 10 \text{ nm}$  with a scanning step size of 10 nm. The frame size of acquired images was  $144 \times 144$  pixels with a readout frequency of 100 frames per second (FPS). HRSTEM image simulation was performed using the multi-slice algorithm, implemented in the STEM-Salabim software package.<sup>[49]</sup> The simulation was carried out by assigning the operating voltage, convergence semi-angle, and aberrations according to the experiments.

## Supporting Information

Supporting Information is available from the Wiley Online Library or from the author.

## Acknowledgements

The authors acknowledge funding by BMBF (Bundesministerium für Bildung und Forschung) in the framework of the FestBatt competence cluster (project 03XP0434B, 03XP0176C, and 03XP0173D).

Open access funding enabled and organized by Projekt DEAL.

## Conflict of Interest

The authors declare no conflict of interest.

## Data Availability Statement

The data that support the findings of this study are available from the corresponding author upon reasonable request.

## Keywords

cathode-solid electrolyte composites, co-sintering, high-resolution STEM, Li-ion batteries, NASICON, olivine cathodes, phase mappings

Received: June 16, 2023

Revised: August 17, 2023

Published online: September 22, 2023

- [1] J. Janek, W. G. Zeier, *Nat. Energy* **2016**, *1*, 16141.
- [2] a) R. Schmich, R. Wagner, G. Hörpel, T. Placke, M. Winter, *Nat. Energy* **2018**, *3*, 267; b) D. Andre, H. Hain, P. Lamp, F. Maglia, B. Stiaszny, *J. Mater. Chem. A* **2017**, *5*, 17174.
- [3] C. Chen, M. Jiang, T. Zhou, L. Rajmakers, E. Vezhlev, B. Wu, T. U. Schüllli, D. L. Danilov, Y. Wei, R.-A. Eichel, P. H. L. Notten, *Adv. Energy Mater.* **2021**, *11*, 2003939.
- [4] S. Randau, D. A. Weber, O. Kötz, R. Koerver, P. Braun, A. Weber, E. Ivers-Tiffée, T. Adermann, J. Kulisch, W. G. Zeier, F. H. Richter, J. Janek, *Nat. Energy* **2020**, *5*, 259.
- [5] a) J. Schnell, T. Günther, T. Knoche, C. Vieider, L. Köhler, A. Just, M. Keller, S. Passerini, G. Reinhart, *J. Power Sources* **2018**, *382*, 160; b) M. Balaish, J. C. Gonzalez-Rosillo, K. J. Kim, Y. Zhu, Z. D. Hood, J. L. M. Rupp, *Nat. Energy* **2021**, *6*, 227.
- [6] E. Umeshbabu, B. Zheng, Y. Yang, *Electrochem. Energy Rev.* **2019**, *2*, 199.
- [7] P. Lu, D. Wu, L. Chen, H. Li, F. Wu, *Electrochem. Energy Rev.* **2022**, *5*.
- [8] a) S. Chen, D. Xie, G. Liu, J. P. Mwizerwa, Q. Zhang, Y. Zhao, X. Xu, X. Yao, *Energy Storage Mater.* **2018**, *14*, 58; b) J. Wu, S. Liu, F. Han, X. Yao, C. Wang, *Adv. Mater.* **2021**, *33*, 2000751; c) J. Wu, L. Shen, Z. Zhang, G. Liu, Z. Wang, D. Zhou, H. Wan, X. Xu, X. Yao, *Electrochem. Energy Rev.* **2021**, *4*, 101.



- [9] a) N. Boaretto, L. Meabe, M. Martinez-Ibañez, M. Armand, H. Zhang, *J. Electrochem. Soc.* **2020**, 167, 070524; b) Y.-H. Chen, Y.-C. Hsieh, K. L. Liu, L. Wichmann, J. H. Thienenkamp, A. Choudhary, D. Bedrov, M. Winter, G. Brunklaus, *Macromol. Rapid Commun.* **2022**, 43, e2200335; c) W. Ren, C. Ding, X. Fu, Y. Huang, *Energy Storage Mater.* **2021**, 34, 515.
- [10] a) F. Zheng, M. Kotobuki, S. Song, M. O. Lai, L. Lu, *J. Power Sources* **2018**, 389, 198; b) M. Pięłowska, B. Kurc, M. Galiński, P. Fuć, M. Kamińska, N. Szymlet, P. Daszkiewicz, *Materials* **2021**, 14.
- [11] Y. Xiao, Y. Wang, S.-H. Bo, J. C. Kim, L. J. Miara, G. Ceder, *Nat. Rev. Mater.* **2020**, 5, 105.
- [12] C. Masquelier, L. Croguennec, *Chem. Rev.* **2013**, 113, 6552.
- [13] A. Manthiram, *Nat. Commun.* **2020**, 11, 1550.
- [14] P. Selinis, F. Farmakis, *J. Electrochem. Soc.* **2022**, 169, 010526.
- [15] L. Miara, A. Windmüller, C.-L. Tsai, W. D. Richards, Q. Ma, S. Uhlenbruck, O. Guillon, G. Ceder, *ACS Appl. Mater. Interfaces* **2016**, 8, 26842.
- [16] M. Gellert, E. Dashjav, D. Grüner, Q. Ma, F. Tietz, *Ionics* **2018**, 24, 1001.
- [17] C.-Y. Yu, J. Choi, V. Anandan, J.-H. Kim, *J. Phys. Chem. C* **2020**, 124, 14963.
- [18] Y. Xiao, L. J. Miara, Y. Wang, G. Ceder, *Joule* **2019**, 3, 1252.
- [19] T. Kato, R. Yoshida, K. Yamamoto, T. Hirayama, M. Motoyama, W. C. West, Y. Iriyama, *J. Power Sources* **2016**, 325, 584.
- [20] J. P. Beaupain, K. Waetzig, S.-K. Otto, A. Henss, J. Janek, M. Malaki, A. Pokle, J. Müller, B. Butz, K. Volz, M. Kuszczak, A. Michaelis, *ACS Appl. Mater. Interfaces* **2021**, 13, 47488.
- [21] M. Malaki, A. Pokle, S.-K. Otto, A. Henss, J. P. Beaupain, A. Beyer, J. Müller, B. Butz, K. Waetzig, M. Kuszczak, J. Janek, K. Volz, *ACS Appl. Energy Mater.* **2022**, 5, 4651.
- [22] Q. Xu, Z. Liu, A. Windmüller, S. Basak, J. Park, K. Dzieciol, C.-L. Tsai, S. Yu, H. Tempel, H. Kungl, R.-A. Eichel, *Small* **2022**, 18, e2200266.
- [23] J. I. Goldstein, D. E. Newbury, J. R. Michael, N. W. Ritchie, J. H. J. Scott, D. C. Joy, *Scanning Electron Microscopy and X-Ray Microanalysis*, Springer, New York **2018**.
- [24] K. Waetzig, A. Rost, C. Heubner, M. Coeler, K. Nikolowski, M. Wolter, J. Schilm, *Alloys Compd.* **2020**, 818, 153237.
- [25] S. J. Pennycook, P. D. Nellist, *Scanning Transmission Electron Microscopy*, Springer, New York **2011**.
- [26] S.-Y. Chung, S.-Y. Choi, T. Yamamoto, Y. Ikuhara, *Phys. Rev. Lett.* **2008**, 100, 125502.
- [27] X. Li, F. Jiang, K. Qu, Y. Wang, Y. Pan, M. Wang, Y. Liu, H. Xu, J. Chen, Y. Huang, J. Zheng, P. Gao, M. Chen, J. Li, Y. Peng, D. Mitlin, *J. Phys. Chem. Lett.* **2020**, 11, 4608.
- [28] A. Mayoral, M. Sanchez-Sanchez, A. Alfayate, J. Perez-Pariente, I. Diaz, *ChemCatChem* **2015**, 7, 3719.
- [29] R. D. Shannon, *Acta Cryst A* **1976**, 32, 751.
- [30] a) B. Ellis, P. Subramanya Herle, Y. H. Rho, L. F. Nazar, R. Dunlap, L. K. Perry, D. H. Ryan, *Faraday Discuss.* **2007**, 134, 119; b) S. P. Ong, L. Wang, B. Kang, G. Ceder, *Chem. Mater.* **2008**, 20, 1798.
- [31] L.-X. Yuan, Z.-H. Wang, W.-X. Zhang, X.-L. Hu, J.-T. Chen, Y.-H. Huang, J. B. Goodenough, *Energy Environ. Sci.* **2011**, 4, 269.
- [32] J. Molenda, in *Metal, Ceramic and Polymeric Composites for Various Uses*, (Ed.: J. Cuppoletti), InTechOpen, Rijeka **2011**.
- [33] E. Zhao, Y. Guo, G. Xu, L. Yuan, J. Liu, X. Li, L. Yang, J. Ma, Y. Li, S. Fan, *J. Alloys Compd.* **2019**, 782, 384.
- [34] S. Hamelet, P. Gibot, M. Casas-Cabanas, D. Bonnin, C. P. Grey, J. Cabana, J.-B. Leriche, J. Rodriguez-Carvajal, M. Courty, S. Levasseur, P. Carlach, M. Van Thournout, J.-M. Tarascon, C. Masquelier, *J. Mater. Chem.* **2009**, 19, 3979.
- [35] S. Hamelet, M. Casas-Cabanas, L. Dupont, C. Davoisne, J. M. Tarascon, C. Masquelier, *Chem. Mater.* **2011**, 23, 32.
- [36] a) A. Paoletta, G. Bertoni, P. Hovington, Z. Feng, R. Flacau, M. Prato, M. Colombo, S. Marras, L. Manna, S. Turner, G. Van Tendeloo, A. Guerfi, G. P. Demopoulos, K. Zaghbi, *Nano Energy* **2015**, 16, 256; b) J. Hu, W. Huang, L. Yang, Feng Pan, *Nanoscale* **2020**, 12, 15036.
- [37] K. M. Ø. Jensen, M. Christensen, H. P. Gunnlaugsson, N. Lock, E. D. Bøjesen, T. Proffen, B. B. Iversen, *Chem. Mater.* **2013**, 25, 2282.
- [38] S.-Y. Chung, S.-Y. Choi, T. Yamamoto, Y. Ikuhara, *Angew. Chem.* **2009**, 121, 551.
- [39] B. Ramasubramanian, S. Sundarajan, V. Chellappan, M. V. Reddy, S. Ramakrishna, K. Zaghbi, *Batteries* **2022**, 8, 133.
- [40] a) H. Liu, C. Li, H. P. Zhang, L. J. Fu, Y. P. Wu, H. Q. Wu, *J. Power Sources* **2006**, 159, 717; b) S. Wang, S. Li, B. Wei, X. Lu, *J. Electrochem. Soc.* **2020**, 167, 100528.
- [41] A. B. Bykov, A. P. Chirkin, L. N. Demyanets, S. N. Doronin, E. A. Genkina, A. K. Ivanov-shits, I. P. Kondratyuk, B. A. Maksimov, O. K. Mel'nikov, L. N. Muradyan, V. I. Simonov, V. A. Timofeeva, *Solid State Ionics* **1990**, 38, 31.
- [42] L. Li, L. Wu, F. Wu, S. Song, X. Zhang, C. Fu, D. Yuan, Y. Xiang, *J. Electrochem. Soc.* **2017**, 164, A2138.
- [43] a) P. Minnmann, F. Strauss, A. Bielefeld, R. Ruess, P. Adelhelm, S. Burkhardt, S. L. Dreyer, E. Trevisanello, H. Ehrenberg, T. Brezesinski, F. H. Richter, J. Janek, *Adv. Energy Mater.* **2022**, 12, 2201425; b) M. Falco, S. Ferrari, G. B. Appetecchi, C. Gerbaldi, *Mol. Syst. Des. Eng.* **2019**, 4, 850.
- [44] L. Vijayan, R. Cheruku, G. Govindaraj, *J. Appl. Phys.* **2012**, 111, 64905.
- [45] M. Catti, A. Cornotti, S. Di Blas, R. M. Ibberson, *J. Mater. Chem.* **2004**, 14, 835.
- [46] M. Sugantha, U. V. Varadaraju, *Solid State Ionics* **1997**, 95, 201.
- [47] C. D. Amos, M. A. Roldan, M. Varela, J. B. Goodenough, P. J. Ferreira, *Nano Lett.* **2016**, 16, 2899.
- [48] L. Jones, H. Yang, T. J. Pennycook, M. S. J. Marshall, S. van Aert, N. D. Browning, M. R. Castell, P. D. Nellist, *Adv Struct Chem Imag* **2015**, 1, 8.
- [49] a) E. J. Kirkland, *Advanced Computing in Electron Microscopy*, Springer US, Boston, MA **2010**; b) J. O. Oelerich, L. Duschek, J. Belz, A. Beyer, S. D. Baranovskii, K. Volz, *Ultramicroscopy* **2017**, 177, 91.